


## Article

# Effect of Powder Formulation and Energy Density on the Nitrogen Content, Microstructure, and Mechanical Properties of SLMed High-Nitrogen Steel

Xin Sun , Jianbiao Ren, Shuhuan Wang and Dingguo Zhao \*

School of Metallurgy and Energy, North China University of Science and Technology, Tangshan 063009, China; sunxin8835@163.com (X.S.)

\* Correspondence: gyyzhao@163.com; Tel.: +86-315-8805020

**Abstract:** The effects of powder formulation, including elemental mixed powder (EMP) and alloy mixed powder (AMP), and energy density on the nitrogen content and microstructural characteristics of high-nitrogen steel prepared by selective laser melting were investigated. The results reveal that the samples prepared with EMP had more nonfusion flaws and a relatively low density, with a maximum of only 92.36%, while samples prepared with AMP had fewer defects and a relative density of up to 97.21%. The nitrogen content and microstructural characteristics were significantly influenced by the laser energy density. The relative density of the EMP samples increased from 88.29% to 92.36% as the laser energy density increased from 83.3 J/mm<sup>3</sup> to 125 J/mm<sup>3</sup>, while the relative density of the AMP samples rose from 93.31% to 97.21%, and the number of defects and the nitrogen content decreased. The mechanical properties of the AMP samples were superior to those of the EMP samples when the energy density rose, and the strength of the high-nitrogen steel first rose and then fell. The AMP samples showed the best mechanical properties when the energy density was 104.2 J/mm<sup>3</sup>, which corresponds to a laser power of 250 W, a scanning speed of 1000 mm/s, and a layer thickness of 30 μm. The corresponding values of yield strength, ultimate tensile strength, and elongation were 958.8 MPa, 1189.2 MPa, and 30.66%, respectively.

**Keywords:** mixed powder; selective laser melting; high-nitrogen steel; mechanical properties



**Citation:** Sun, X.; Ren, J.; Wang, S.; Zhao, D. Effect of Powder Formulation and Energy Density on the Nitrogen Content, Microstructure, and Mechanical Properties of SLMed High-Nitrogen Steel. *Processes* **2023**, *11*, 1937. <https://doi.org/10.3390/pr11071937>

Academic Editor: Carlos Sierra Fernández

Received: 7 June 2023  
Revised: 24 June 2023  
Accepted: 25 June 2023  
Published: 27 June 2023



**Copyright:** © 2023 by the authors. Licensee MDPI, Basel, Switzerland. This article is an open access article distributed under the terms and conditions of the Creative Commons Attribution (CC BY) license (<https://creativecommons.org/licenses/by/4.0/>).

## 1. Introduction

Nitrogen has long been regarded as one of the harmful impurities in traditional steel. However, in the early 20th century, researchers discovered that the addition of a certain amount of nitrogen could influence the mechanical properties of steel and the stability of the austenite phase region. This finding sparked a wave of research on nitrogen-containing stainless steels, and it gradually gained recognition in the field [1–3]. Despite the growing acceptance of high-nitrogen stainless steel, there is no unified standard for its definition. Speidel [4] considers “high-nitrogen steel” to be steel with a nitrogen content exceeding the limit achievable under normal pressure (0.1 MPa). However, the classification of nitrogen-containing stainless steel depends on the mass fraction of nitrogen in austenitic stainless steel. It can be divided into three types: the nitrogen-controlled type (0.05 wt% to 0.10 wt%), the medium-nitrogen type (0.10 wt% to 0.40 wt%), and the high-nitrogen type (above 0.40 wt%). For ferritic stainless steel and martensitic-matrix stainless steel, a nitrogen content exceeding 0.08% can be referred to as high-nitrogen steel. Furthermore, based on their microstructures, high-nitrogen steels can be categorized into five main types: nitrogen-containing austenitic stainless steel, nitrogen-containing duplex stainless steel, nitrogen-containing ferritic stainless steel, nitrogen-containing martensitic stainless steel, and nitrogen-containing precipitation-hardened stainless steel [5]. High-nitrogen steel is an innovative type of stainless steel that offers significant advantages, such as a low cost and high strength, by utilizing inexpensive nitrogen elements to replace expensive nickel.

By adding nitrogen as interstitial atoms to the stainless-steel matrix, the solid solution is strengthened, resulting in improved strength, toughness, and corrosion resistance [6,7]. These outstanding properties have made high-nitrogen steel increasingly popular in various industries, including the bioenergy industry, aerospace industry, petrochemical industry, marine engineering, biomedical applications, and others [8,9]. The utilization of high-nitrogen steel has revolutionized these industries, offering enhanced performance and cost-effectiveness as compared to traditional stainless steels. In the bioenergy industry, for example, high-nitrogen steel components exhibit excellent resistance to corrosion and fatigue, making them ideal for critical applications in biofuel production and processing. In the aerospace sector, the high strength of high-nitrogen steel enables the construction of lightweight structures without compromising safety and reliability. Similarly, in the petrochemical industry, the superior corrosion resistance of high-nitrogen steel ensures the durability and longevity of equipment exposed to harsh chemical environments. Moreover, high-nitrogen steel finds extensive use in marine engineering, where its enhanced strength and corrosion resistance make it suitable for shipbuilding, offshore platforms, and underwater structures. In the biomedical field, high-nitrogen steel's biocompatibility and corrosion resistance make it an excellent choice for medical devices, implants, and surgical instruments, where durability and long-term performance are paramount [9–13].

Supersaturated nitrogen can be added to steel to significantly increase its strength, according to the research [8]. The insufficient solubility of nitrogen in iron-based materials at atmospheric pressure makes the production of high-nitrogen steel challenging. At 1 standard atmospheric pressure and 1600 °C, the solubility is only 0.045 wt% [14]. The solubility and distribution uniformity of nitrogen during the steel solidification process are therefore improved by applying pressure, which is typically done using high-pressure technology [15]. High-nitrogen steel can only be produced on a large scale because the equipment and method required to prepare it under high pressure are complicated, dangerous, and expensive. In addition, strain strengthening happens due to cast high-nitrogen steel's relatively high hardness. While strain strengthening occurs throughout the manufacturing process, the hardness of cast high-nitrogen steel is also rather high, making typical machining more challenging [16].

Metal additive manufacturing (MAM), also known as metal 3D printing, is a revolutionary manufacturing technology that emerged in the 1980s. It uses digital model files and metal powder as the processing material, and it prints layer by layer using a high-energy heat source, enabling the fast and moldless fabrication of complex components [17]. Its low material consumption, high processing efficiency, and capacity for achieving integrated structures have drawn significant attention from researchers, making it one of the most popular topics in the manufacturing industry [18]. Metal additive manufacturing has developed into various shaping techniques, classified by different heat sources. These include laser engineered net shaping (LENS), electron beam selective melting (EBSM), selective laser sintering (SLS), and selective laser melting (SLM). These techniques have been widely applied and advanced abroad, forming mature and large-scale systems [19]. Metal materials for additive manufacturing have been explored both domestically and internationally, covering a broad spectrum of alloys, such as titanium-based alloys [20,21], nickel-based alloys [22,23], iron-based alloys [24], aluminum alloys [25], and high-entropy alloys [26]. These materials have unique properties and performance features that suit different applications. Metal additive manufacturing is a significant breakthrough in the field of manufacturing technology in the past 30 years and is considered to be a key driver of the third industrial revolution. It has advantages, such as producing complex geometries, customizing designs, and integrating functions, that have changed traditional manufacturing processes and opened up new possibilities for product development and production [27]. With continuous improvement and increasing research and development efforts, metal additive manufacturing is expected to play an increasingly important role in various industries, such as aerospace, automotive, medical, and consumer goods, revolutionizing the way we design and manufacture components [28–30]. The ability to net-form

parts using metal additive manufacturing is possible [31], greatly reducing the difficulty of subsequent processing and enabling the processing of high-nitrogen steel. By simultaneously feeding wire powder and a TIG arc additive, Wu et al. [32] formed a straight wall made of high-nitrogen steel, and the nitrogen content was greatly raised by adding Cr<sub>2</sub>N powder, yielding a nitrogen content of 1.04%. Unfortunately, the droplets react with the air during the arc additive process, which lends a susceptibility to flaws, such as inclusions and porosity.

In order to effectively remove the defects, such as oxidation inclusions and pores during the AM process, selected laser melting has a protective gas compartment that can be filled with nitrogen or argon gas with a purity value of 99.999%. In the selective laser melting (SLM) process, metal powder is the most basic and crucial raw material. In theory, any powder that can be melted and metallurgically bonded using a laser heat source can be used for SLM forming. However, in practice, SLM differs from traditional powder metallurgy as the morphology, sphericity, particle size distribution, and flowability of metal powders can all affect the formability of SLM parts. This requires the metal powder to have excellent properties, such as particle size, sphericity, and purity [33,34]. Lv et al. [35,36] investigated the advantages of selective laser melting, which may be used to create complicated parts, including high forming precision and precise positioning. Using home-made, aerosolized, high-nitrogen steel powder is one way to conduct the selective laser melting process of high-nitrogen steel. However, the preparation of high-nitrogen steel powder is expensive and complicated. Thus, it is urgent to find a new method for preparing high-nitrogen steel.

In order to obtain powders with a nitrogen content much higher than the permissible nitrogen content (0.4 wt%), and to effectively reduce the production cost of the powder, our research method adds chromium nitride powder to the premixed powder. The effects of powder formulation, including elemental mixed powder (EMP) and alloy mixed powder (AMP), and energy density on the nitrogen content and microstructural characteristics of high-nitrogen steel prepared by selective laser melting were investigated. The relevant research results can provide guidance for the selective laser melting of high-nitrogen steel in engineering.

## 2. Materials and Methods

The distribution of the particle sizes was between 15 and 53  $\mu\text{m}$ . To create the mixed powder, the elemental powder and alloy powder were first mixed separately. Mixed powder is defined as a powder with a nitrogen content significantly higher than the maximum nitrogen content of 0.4 wt% in steel under atmospheric pressure. Iron powder, chromium nitride, chromium powder, manganese powder, and molybdenum powder with a purity of higher than 99.0% were used as raw ingredients for the elemental mixed powders (EMPs). While CrN and Mn are asymmetric powders; Fe, Cr, and Mo are spherical powders. To calculate the weight of each metal powder, we used the following formula: Fe: Cr: Mn: Mo: CrN = 63:12:12:3:10 per 100 g. At a ratio of 98:2 per 100 g, alloy mixed powders (AMP) were prepared from spherical stainless-steel powder with a nitrogen content of 0.29 wt% and a nonspherical chromium nitride powder with a purity of 99.0%. Table 1 provides the chemical composition of the mixed powders.

**Table 1.** Chemical composition of the mixed powders (wt%).

Elements	Cr	Mn	Mo	N	C	Fe
EMP	20.53	10.61	3.23	1.472	0.038	Bal
AMP	21.14	11.21	3.04	1.01	0.036	Bal

Following weighing, the powder was first extensively combined in a planetary ball mill for 4 h at a speed of 400 rpm. The ball mill tank was sealed and vacuum treated for 10 min before being mixed to lessen oxidation. Two different types of mixed powders were

evaluated for flowability, apparent density, and compacted density, and the corresponding findings are displayed in Table 2. The particle size distribution of the mixed powder was measured using a laser diffraction particle size distribution meter, and the results are displayed in Figure 1. The D10, D50, and D90 of the EMP were 20.31, 36.57, and 58.35  $\mu\text{m}$ , respectively, and the average particle size was 36.57  $\mu\text{m}$ . The D10, D50, and D90 of the AMP were 21.91, 34.23, and 53.25  $\mu\text{m}$ , respectively. Both kinds of powders met the specifications for particle size distribution for selective laser melting, with an average particle size of 34.23  $\mu\text{m}$ .

**Table 2.** Comparison of the characteristics of the mixed powders.

Mixed Powder	Size ( $\mu\text{m}$ )	Flowability (s/50 g)	Apparent Density ( $\text{g}/\text{cm}^3$ )	Compacted Density ( $\text{g}/\text{cm}^3$ )
EMP	15-53	40.25	3.44	3.85
AMP	15-53	29.81	4.15	4.36

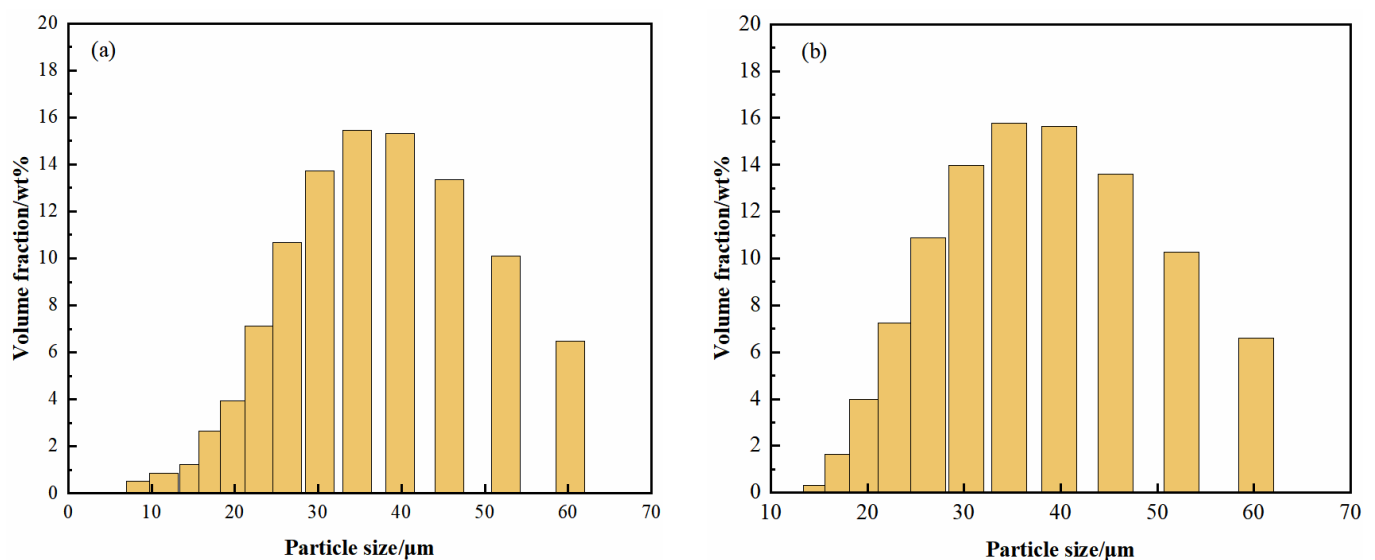


**Figure 1.** Particle size distribution of the mixed powders: (a) EMP; (b) AMP.

DiMetal-280 equipment with a substrate preheating temperature of 150  $^{\circ}\text{C}$  and a forming chamber covered by nitrogen gas was used for selective laser melting. The powder layer thickness was 30  $\mu\text{m}$  for the selective laser melting. The scan interval was 80  $\mu\text{m}$ , the scanning speed was 1000 mm/s, and the laser power was 200, 225, 250, 275, and 300 W, respectively. The corresponding laser energy densities were 83.3, 93.8, 104.1, 114.6, and 125.0  $\text{J}/\text{mm}^3$ , respectively. The tensile specimen is shown in Figure 2. The block sample had dimensions of 5  $\times$  5  $\times$  5 mm. It was intended for room-temperature tensile testing according to GB/T 228.1-2021.

The morphology and elemental distribution of the powder, as well as the pore flaws, microstructure, and tensile fracture surface of the samples, were examined using optical microscopy and a Czech TESCAN MIRA LMS SEM. The Archimedes drainage method was used to calculate the samples' relative density. The nitrogen content was measured by using a LECO oxygen, nitrogen, and hydrogen analyzer. Tensile testing was performed at room temperature using CMT4204 static hydraulic universal testing equipment to measure tensile strength, yield strength, and elongation.

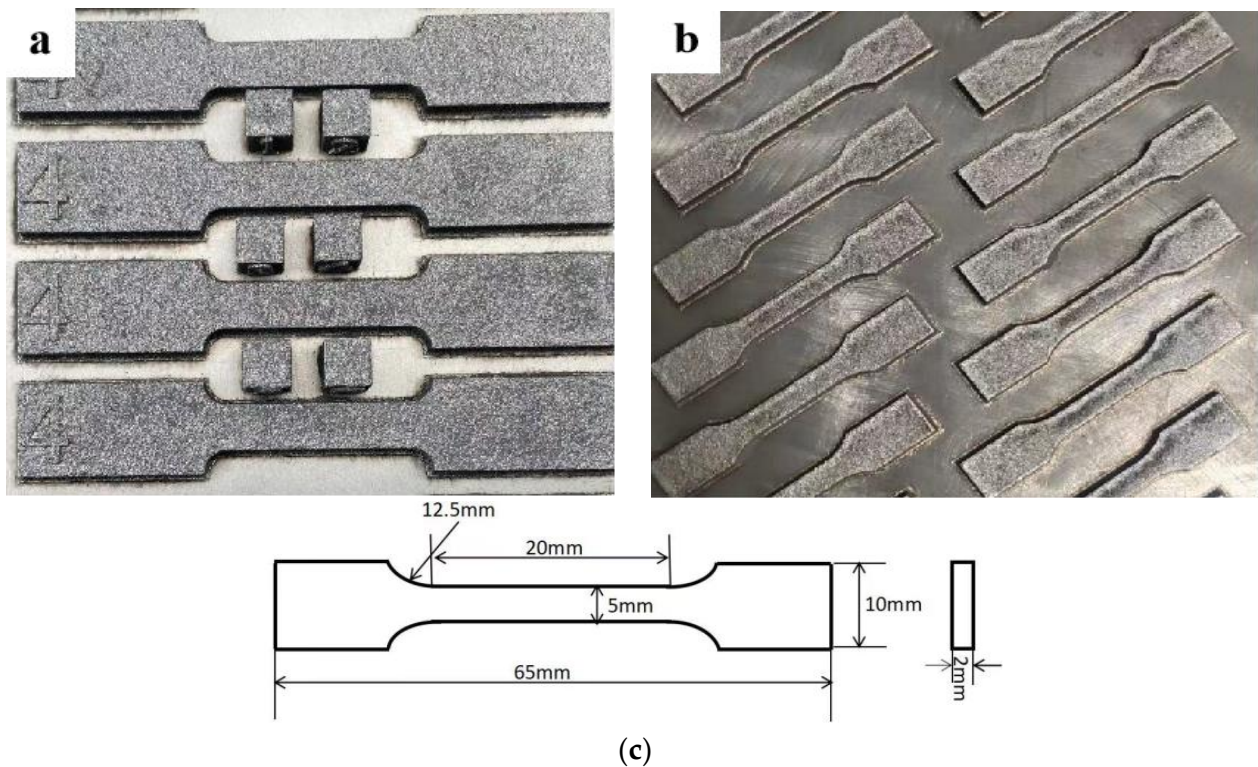


**Figure 2.** The SLMed samples prepared by: (a) EMP and (b) AMP; (c) Schematic diagram of tensile specimen dimensions.

### 3. Results and Discussion

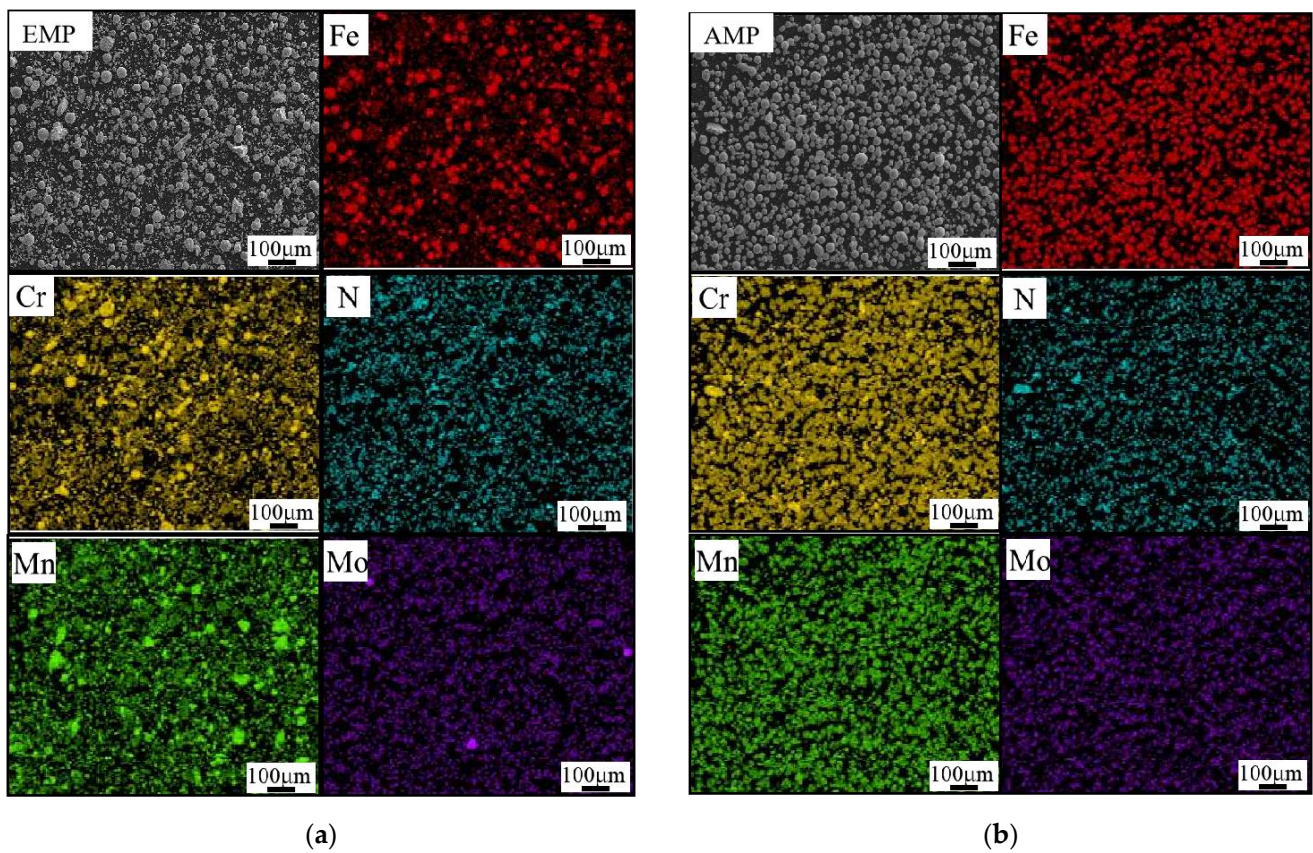
#### 3.1. Morphological Characteristics and Elemental Distribution of the Mixed Powder

In Figure 3, the two powders' morphologies and elemental distributions are depicted. The results demonstrate that the sphericity of the EMP was poor, and there were numerous nonspherical powder particles, while there was only a very small amount of nonspherical powder in the AMP. There was a small amount of aggregation in the elemental distribution of the EMP, while the elemental energy spectrum scanning results of the AMP were more uniform. This might be a result of the alloy mixed powder having greater flowability, apparent density, and compacted density due to the use of more irregular powders, specifically CrN and Mn, which accounted for up to 22% of the total, and which have uneven particle sizes distributed throughout, as shown in Table 2.

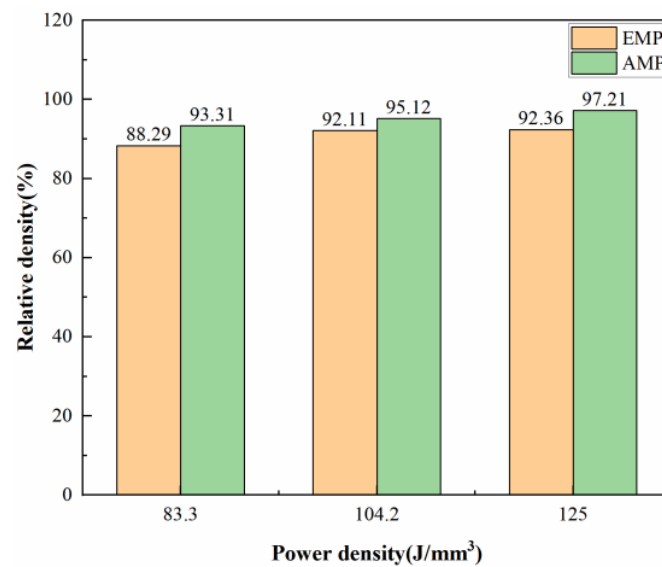
#### 3.2. The Effect of Powder Formulation and Energy Density on the Relative Density of High-Nitrogen Steel

Figure 4 shows the relative density of the EMP and AMP samples under different energy densities. The results demonstrate that, as the energy density increased, the relative density of the two samples increased, and that the density of the AMP samples was superior to that of the EMP samples. When the energy density was  $104.2 \text{ J/mm}^3$ , the relative density of the AMP samples reached 97.21%, while it was only 92.36% for the EMP samples. Theoretical studies have demonstrated that, when the laser energy density is low, the actual printing temperature is effectively improved as the laser energy density rises, greatly improving the density of the printed samples [37]. The behavior of the powder and the relative density can both be impacted by the flowability and apparent density of the powder [38,39]. With an increase in energy density, the relative density of the two samples rose. This happened as the density of the samples grew; both the energy density and the energy absorbed by the powder increased. As a result, the powder totally melted, and the fluidity in the micro melt pool increased. However, since the gas could not be entirely expelled during printing, the density was significantly reduced, and more gas was

created in the micro melt pool due to the large amount of fine powder, poor fluidity, and low apparent density of the EMP.



**Figure 3.** Comparison of the morphology and element distribution of the mixed powders: (a) EMP and (b) AMP.



**Figure 4.** Relative density [40] of the EMP and AMP samples under different energy density conditions.

### 3.3. The Effect of Powder Formulation and Energy Density on the Microstructure of the High-Nitrogen Steel

Figure 5 displays the microstructure of the samples prepared with the EMP and AMP. Both types of samples had numerous pore flaws, as shown in Figure 5a–f. While there

were few flaws and a smooth edge to the faults in the AMP samples, there were more nonfusion defects and spheroidized particles in the EMP samples. Meanwhile, nonfusion defects also appeared when the energy density was low. When the melt pool's temperature is low, the liquid-phase dynamic viscosity is high; thus, the melt's fluidity is low and the wettability between the melt and the matrix is low [41]. When the energy density is low, as demonstrated by [42], the metal in the micro melt pool cools quickly. As liquid metal solidifies before the bubbles have a chance to leave the surface of the micro melt pool, they can shape themselves into virtually circular pores. With an increase in energy density, the phenomenon of nonfusion in the two samples improves since increasing energy density improves the melt's fluidity and wettability with the substrate. Yet, the morphology of the two types of samples differed at the same power because of the two powders' inconsistent sphericity, fluidity, and elemental homogeneity.

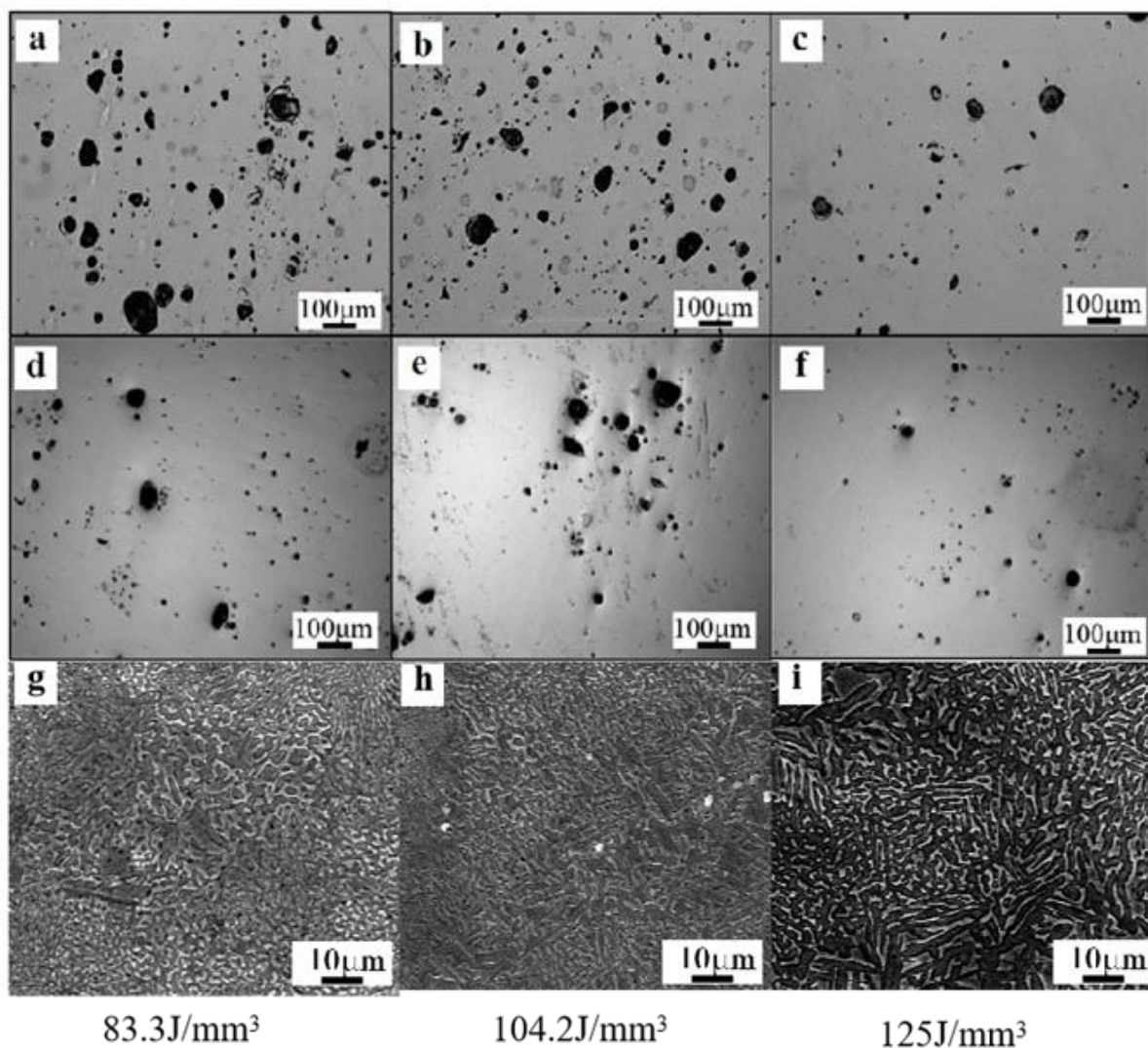


**Figure 5.** Comparison of the defects in samples prepared with: (a–c) EMP and (d–i) AMP.

In order to obtain a clearer observation of the morphological structure of the samples under three different energy densities, scanning electron microscopy (SEM) was utilized to scan the samples. The columnar and cellular crystals made up the microstructure of the AMP samples, as can be seen in Figure 5g–i. The cellular and columnar crystals gradually became coarser as the energy density rose. Theoretical studies have demonstrated that increasing both the volume energy density [43] and the surface energy density inputs into the molten pool [44] will result in an increase in the size of the cellular structure [45]. Due

to the relatively high temperature gradient and rapid solidification of the alloy mixed powder during the SLM process, cellular dendrites, instead of planar crystals, preferentially developed in the SLM material. The microstructure was therefore found to have cellular structures [46]. The molten pool's temperature rises as the energy density does as well, and as the laser strength rises, the temperature of the molten pool rises and prolongs the existence of the molten pool, which favors crystal growth. As a result, the cellular crystals tend to grow in size, while the columnar crystals progressively become coarser.

Figure 6 depicts the results of the composition analysis of the EMP samples. It was discovered that the spheroidized particles were made up of elemental elements including Mo and Cr in the matrix. Unfused particles and element aggregation in the EMP samples were the product of the uneven distribution of elemental elements in the powder. When comparing the microstructure and morphology of the two samples, it can be seen that both improved with increases in the energy density. However, the morphology of the EMP samples was less complete than that of the AMP samples, and the improvement in morphology was greater with increases in the energy density. In order to produce samples with a higher nitrogen content and better morphology, it is necessary to fully consider the quality of the powder while considering the nitrogen content when configuring two different types of mixed powder samples.

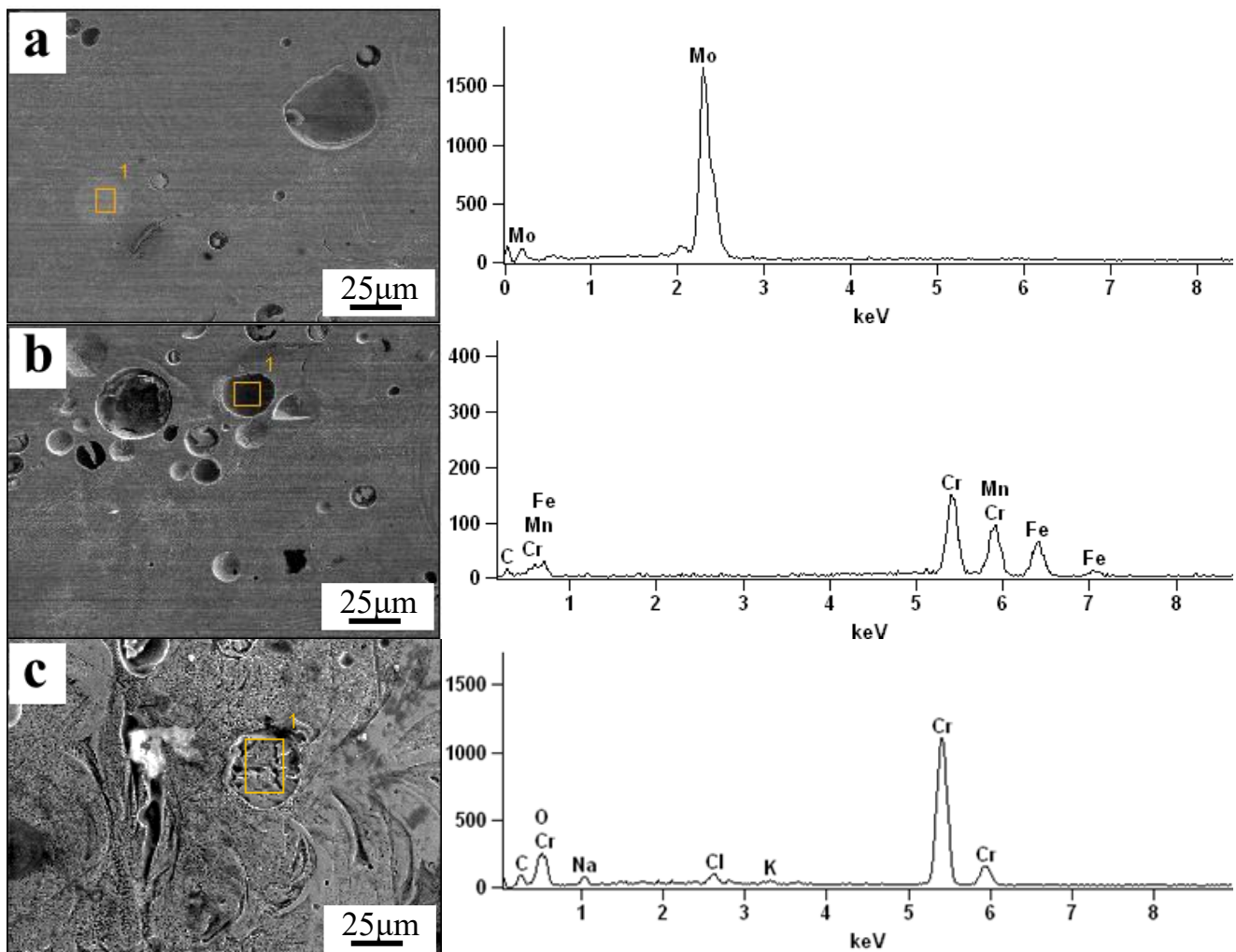


**Figure 6.** Composition analysis of the samples prepared with EMP: (a) unmelting particles of Mo; (b) unmelting particles of Fe, Cr, and Mn compounds; (c) unmelting particles of Cr.



### 3.4. The Effect of Powder Formulation and Energy Density on the Microstructure of the High-Nitrogen Steel

Figure 7 depicts the relationship between the nitrogen content in the EMP and AMP samples and the energy density. It can be seen that the nitrogen content of the EMP samples decreased from 0.996 wt% to 0.96 wt%, and the nitrogen loss rate rose from 32.34% to 34.78% when the energy density increased from 83.3 J/mm<sup>3</sup> to 125 J/mm<sup>3</sup>. The nitrogen content of the AMP samples decreased from 0.836 wt% to 0.768 wt%, and the nitrogen loss rate rose from 17.23% to 23.96%. When the energy density was increased, the nitrogen contents of the two types of samples dropped by 0.036 wt% and 0.068 wt%, respectively, and the nitrogen loss rate rose by 2.44% and 6.73%, respectively. As the energy density rose, the nitrogen content gradually declined, and the nitrogen loss rate gradually rose. Although the nitrogen loss rate increased with the increase of initial nitrogen content in the powder, it is possible to obtain high-nitrogen steel samples above 0.4 wt% through powder blending under atmospheric-pressure printing conditions.

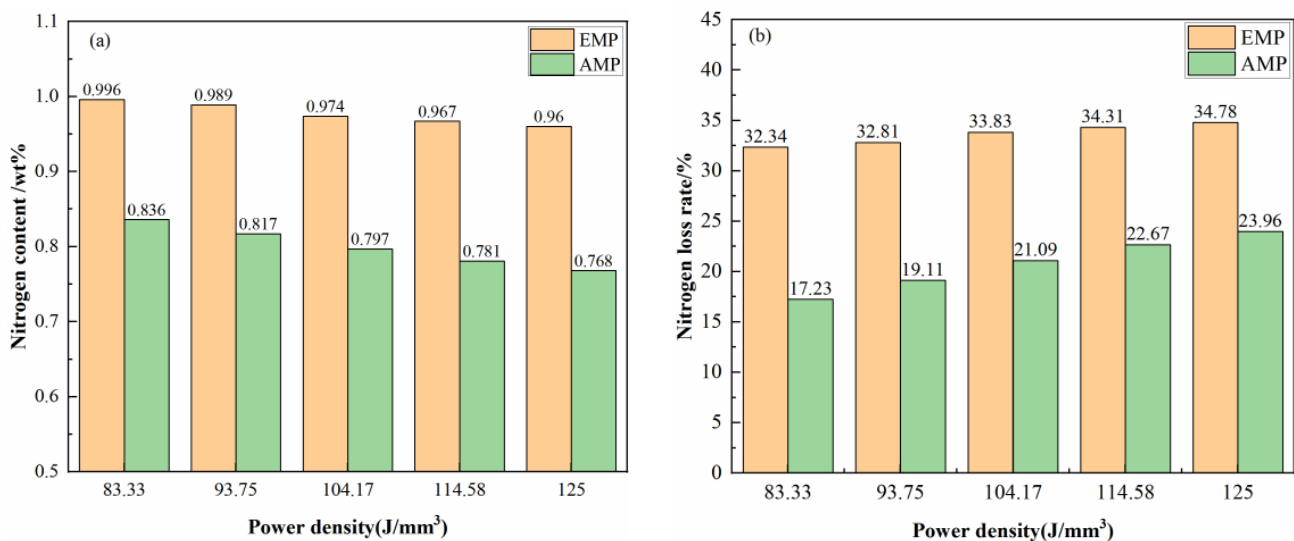


**Figure 7.** Comparison of nitrogen content of the formed samples under different energy densities: (a) Nitrogen content and (b) Nitrogen loss rate.

In conclusion, it is clear that a lower laser energy density can successfully prevent nitrogen escape. It is hypothesized that the cause is that, when the molten pool's nitrogen content is supersaturated, the lower energy density accelerates the micro molten pool's solidification process. As a result, the gas cannot escape before the molten pool solidifies, effectively reducing nitrogen loss. Under the same printing conditions, EMP with a higher initial nitrogen content can produce a sample with a higher nitrogen content, but it will also result in a higher nitrogen loss, suggesting that a sample's nitrogen content can be increased by increasing the initial nitrogen content of the mixed powder.

### 3.5. Mechanical Properties of the High-Nitrogen Steel

The mechanical properties of the EMP and AMP samples were examined under various energy density conditions. The typical tensile curves are displayed in Figure 8. The results show that the AMP samples had mechanical properties (yield strength, tensile strength, and elongation) superior to those of the EMP samples. The equivalent comparison of yield strength and tensile strength is shown in Figure 9. When the energy density was 114.6 J/mm<sup>3</sup>, the EMP samples had the highest ultimate tensile strength, at 1005.74 MPa; when the energy density was 105 J/mm<sup>3</sup>, the AMP samples had the highest ultimate tensile strength, at 1189.2 MPa. As the energy density increased, the tensile strength of the two samples first increased and then decreased. At each energy density, the strength of the AMP samples was greater than that of the EMP samples. The equivalent elongation comparison

is shown in Figure 10. The EMP samples had the greatest elongation, 13.07%, at the energy density of 300 W. The elongation of the AMP samples was above 24%, which was much better than that of the EMP samples.

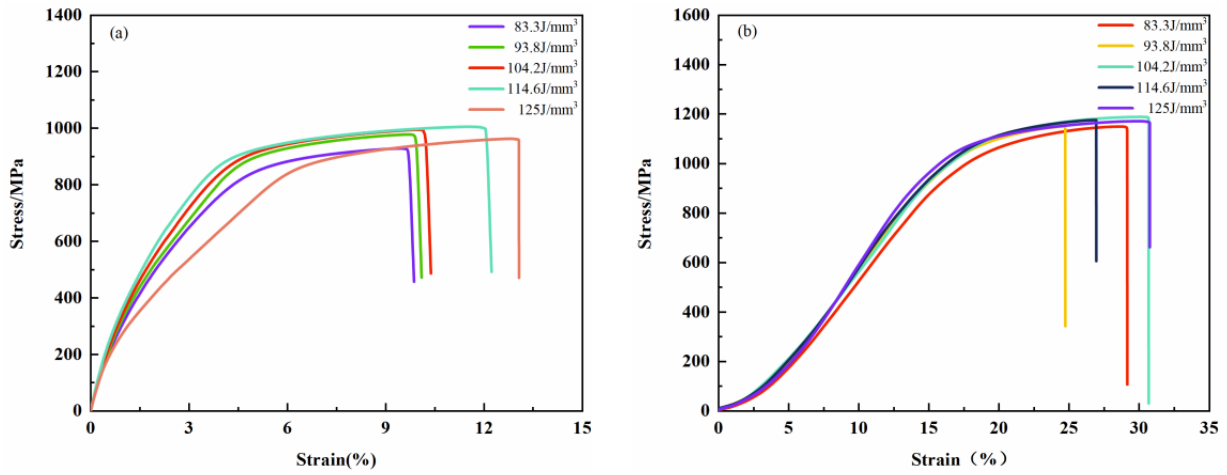


Figure 8. Typical stress–strain curves under different energy density conditions: (a) sample formed from EMP and (b) sample formed from AMP.

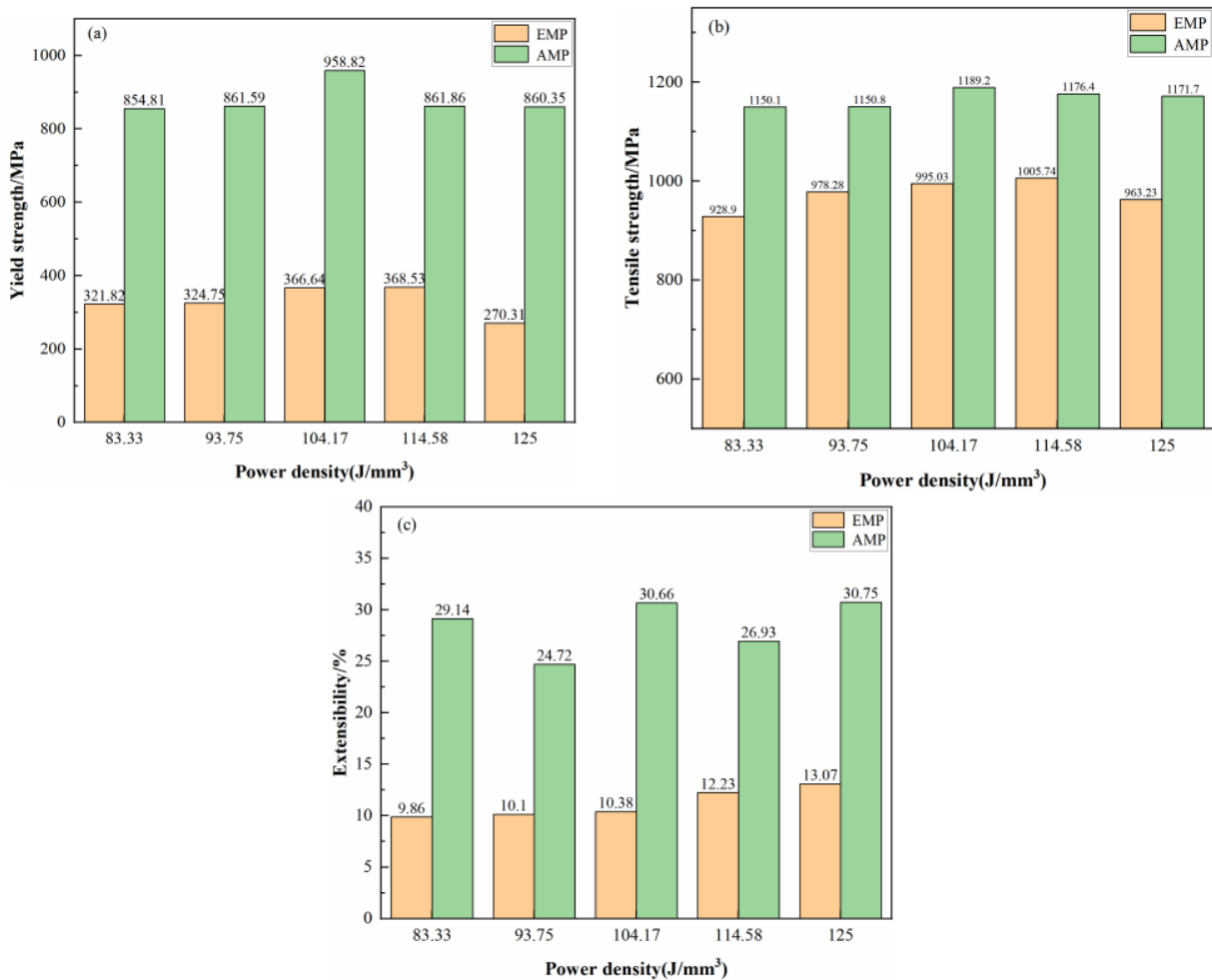
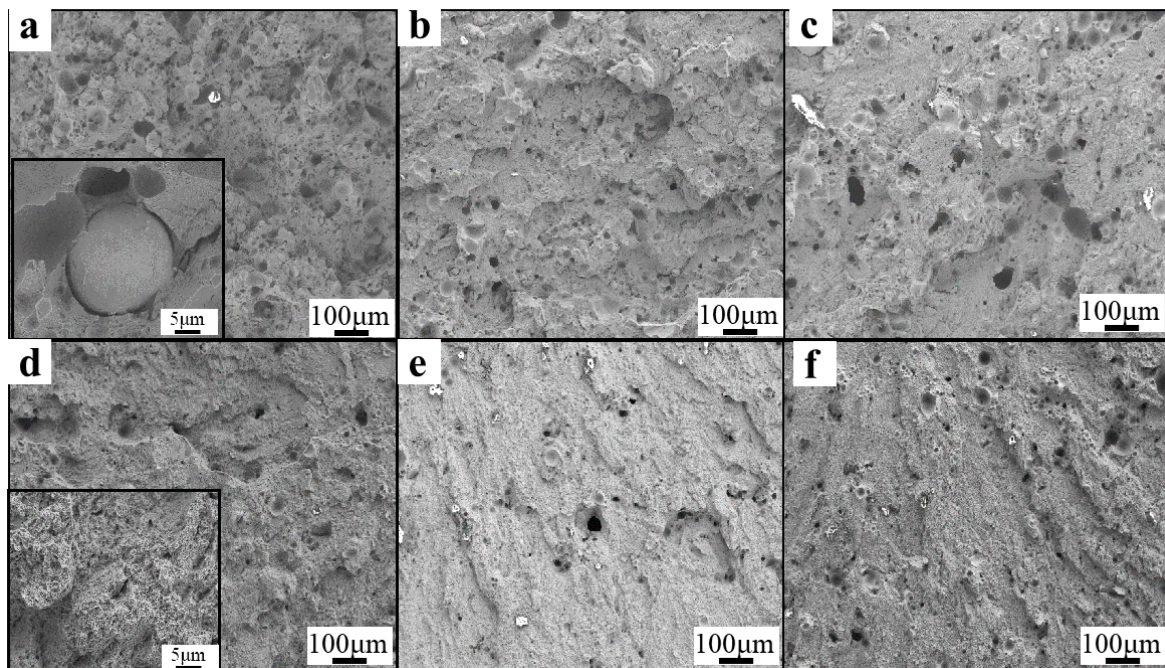


Figure 9. Comparison of YS, UTS, and elongation of the formed samples under different energy densities: (a) yield strength; (b) tensile strength; (c) extensibility.



**Figure 10.** Fracture morphology of tensile specimens prepared with: (a–c) EMP and with (d–f) AMP.

The above-described research indicates that the steel's strength can be greatly increased by the nitrogen in high-nitrogen steel by acting as solid solution strengthening [47]. The Hall–Petch relationship [48] states that the strength of the metal will diminish as the grain size increases, and that the absence of fusion (pores) will diminish the sample's tensile properties [49]. A positive correlation exists between strength and high or low density [50]. As the energy density rose, the nitrogen content decreased, while the size of the samples' grains grew. The samples' unfused defects progressively worsened as the energy density was increased. When a number of variables are coupled together, the strength is low. The samples' absence of fusion flaws gradually declined as the energy density rose, and the strength gradually rose. An increase in pores inside the samples and the disruption of the matrix continuity occur when the power is too high because these factors cause the micro melt pool to evaporate more quickly and the keyhole changes considerably in size. In the end, the energy density does not continue to grow. The EMP samples exhibited numerous incomplete fusion defects and spheroidized particles, as shown in Figure 5. Despite the higher nitrogen content of the EMP samples, the strength was significantly lower than that of the AMP samples.

Figure 10 displays the fracture morphology of the two types of samples under various energy density conditions. On the fracture surface of the EMP samples, there were numerous spheroidized substances with a size of 25  $\mu\text{m}$  and pore defects. There were only a few dimples, and the predominant fracture mode was that of brittle fracture. Consequently, the ductility was not very high. On the other hand, the fracture morphology of the AMP samples (Figure 10d–f) contained numerous dimples, a negligible number of pore flaws, and no signs of spheroidization, indicating ductile fractures. Compared to that of the EMP samples, the ductility of the AMP samples was markedly enhanced because the EMP samples had a high percentage of nonspherical powder, poor flowability, and an uneven element distribution.

#### 4. Conclusions

The nitrogen content, microstructure, and mechanical properties of high-nitrogen steel prepared using selective laser melting were investigated in this study, along with the impacts of powder formulation (elemental mixed powder and alloy mixed powder) and energy density. The main conclusions are as follow:

- (1) The formulation of mixed powders significantly affects the quality of high-nitrogen steel. The samples prepared with EMP had more nonfusion flaws and a relatively low density, with a maximum of only 92.36%, while the samples prepared with AMP had fewer defects and a density of up to 97.21%. This is due to the uneven distribution of elements, poor sphericity, and poor flowability of the elemental mixed powder.
- (2) The nitrogen content and microstructural characteristics are significantly influenced by the laser energy density. The relative density of the EMP samples increased from 88.29% to 92.36% with the increase in laser energy density from 83.3 J/mm<sup>3</sup> to 125.0 J/mm<sup>3</sup>, while the relative density of the AMP samples increased from 93.31% to 97.21%, and it contained fewer defects and a lower nitrogen content.
- (3) The mechanical properties of the AMP samples were superior to those of the EMP samples when the energy density rose, and the strength of the high-nitrogen steel first rose and then fell. The AMP samples possessed the best mechanical properties when the energy density was 104.2 J/mm<sup>3</sup>, which corresponds to a laser power of 250 W, a scanning speed of 1000 mm/s, and layer thickness of a 30 µm. These values of yield strength, tensile strength, and elongation were 958.8 MPa, 1189.2 MPa, and 30.66%, respectively.

**Author Contributions:** Conceptualization, D.Z.; methodology, S.W.; formal analysis, X.S.; investigation, J.R.; writing—original draft preparation, X.S.; writing—review and editing, X.S. All authors have read and agreed to the published version of the manuscript.

**Funding:** The current work was supported by the Central Guidance on Local Science and Technology Development Fund of Hebei Province (226Z1008G), the National Natural Science Foundation of China (No. 52274336), and the Research Project of Basic Scientific Research Expenses of Hebei Province (No. JYG2021004).

**Data Availability Statement:** No new data were created or analyzed in this study. Data sharing is not applicable to this article.

**Conflicts of Interest:** The authors declare no conflict of interest.

## References

1. Degallaix, S.; Foct, J.; Hendry, A. Mechanical Behaviour of High-Nitrogen Stainless Steels. *Mater. Sci. Technol.* **1986**, *2*, 946–950. [[CrossRef](#)]
2. Li, H.; Jiang, Z.; Zhang, Z.; Xu, B.; Liu, F. Mechanical Properties of Nickel Free High Nitrogen Austenitic Stainless Steels. *J. Iron Steel Res. Int.* **2007**, *14*, 330–334. [[CrossRef](#)]
3. Chai, G.; Siriki, R.; Nordström, J.; Dong, Z.; Vitos, L. Roles of Nitrogen on TWIP in Advanced Austenitic Stainless Steels. *Steel Res. Int.* **2022**, 2200359. [[CrossRef](#)]
4. Speidel, H.J.; Speidel, M.O. Nickel and Chromium-Based High Nitrogen Alloys. *Mater. Manuf. Process.* **2004**, *19*, 95–109. [[CrossRef](#)]
5. Rashev, T.V.; Eliseev, A.V.; Zhekova, L.T.; Bogev, P.V. High-Nitrogen Steel. *Steel Transl.* **2019**, *49*, 433–439. [[CrossRef](#)]
6. Li, S.; Zhang, C.; Lu, J.; Chen, R.; Chen, D.; Cui, G. A Review of Progress on High Nitrogen Austenitic Stainless-Steel: Ingenta Connect. *Mater. Express* **2021**, *11*, 1901–1925. [[CrossRef](#)]
7. Di Schino, A.; Kenny, J.M. Grain Refinement Strengthening of a Micro-Crystalline High Nitrogen Austenitic Stainless Steel. *Mater. Lett.* **2003**, *57*, 1830–1834. [[CrossRef](#)]
8. Li, H.; Jiang, Z.; Feng, H.; Ma, Q.; Zhan, D. Aging Precipitation Behavior of 18Cr-16Mn-2Mo-1. 1N High Nitrogen Austenitic Stainless Steel and Its Influences on Mechanical Properties. *J. Iron Steel Res. Int.* **2012**, *19*, 43–51. [[CrossRef](#)]
9. Xia, L.; Li, H.; Feng, H.; Jiang, Z.; Zhu, H.; Zhang, S.; Wang, X. Enhanced Strength and Toughness of High Nitrogen Stainless Bearing Steel by Controlling Interstitial Partitioning via V-Microalloying. *J. Mater. Sci. Technol.* **2023**, *151*, 204–218. [[CrossRef](#)]
10. Anderson, M.C.; Shin, Y.C. Laser-Assisted Machining of an Austenitic Stainless Steel: P550. *Proc. Inst. Mech. Eng. Part B J. Eng. Manuf.* **2006**, *220*, 2055–2067. [[CrossRef](#)]
11. Kuznetsov, Y.V.; Muradyan, O.S.; Muradyan, S.O. Development of High-Strength Corrosion Resistant Austenitic Steel for Oil Equipment Shafts. *Metallurgist* **2022**, *65*, 1095–1099. [[CrossRef](#)]
12. High-Manganese and Nitrogen Stabilized Austenitic Stainless Steel (Fe–18Cr–22Mn–0.65N): A Material with a Bright Future for Orthopedic Implant Devices—IOPscience. Available online: <https://iopscience.iop.org/article/10.1088/1748-605X/ac265e/meta> (accessed on 21 June 2023).
13. Radice, S.; Impergre, A.; Fischer, A.; Wimmer, M.A. Corrosion Resistance of the Nickel-free High-nitrogen Steel FeCrMnMoN0.9 under Simulated Inflammatory Conditions. *J. Biomed. Mater. Res. Part B Appl. Biomater.* **2021**, *109*, 902–910. [[CrossRef](#)] [[PubMed](#)]

14. Simmons, J.W. Overview: High-Nitrogen Alloying of Stainless Steels. *Mater. Sci. Eng. A* **1996**, *207*, 159–169. [[CrossRef](#)]
15. Preparation of Cr17Mn11Mo3N Powders by High-Pressure Gas Atomization and the Nitrogen Increasing Mechanism—ScienceDirect. Available online: <https://www.sciencedirect.com/science/article/abs/pii/S0032591021002163> (accessed on 21 June 2023).
16. Cheng, B.; Wei, F.; Teh, W.H.; Lee, J.J.; Meng, T.L.; Lau, K.B.; Chew, L.T.; Zhang, Z.; Cheong, K.H.; Ng, C.K.; et al. Ambient Pressure Fabrication of Ni-Free High Nitrogen Austenitic Stainless Steel Using Laser Powder Bed Fusion Method. *Addit. Manuf.* **2022**, *55*, 102810. [[CrossRef](#)]
17. Armstrong, M.; Mehrabi, H.; Naveed, N. An Overview of Modern Metal Additive Manufacturing Technology. *J. Manuf. Process.* **2022**, *84*, 1001–1029. [[CrossRef](#)]
18. Full Article: Topology Optimization for Metal Additive Manufacturing: Current Trends, Challenges, and Future Outlook. Available online: <https://www.tandfonline.com/doi/full/10.1080/17452759.2023.2181192> (accessed on 21 June 2023).
19. Frazier, W.E. Metal Additive Manufacturing: A Review. *J. Mater. Eng. Perform.* **2014**, *23*, 1917–1928. [[CrossRef](#)]
20. Attar, H.; Ehtemam-Haghighi, S.; Kent, D.; Dargusch, M.S. Recent Developments and Opportunities in Additive Manufacturing of Titanium-Based Matrix Composites: A Review. *Int. J. Mach. Tools Manuf.* **2018**, *133*, 85–102. [[CrossRef](#)]
21. Tong, J.; Bowen, C.R.; Persson, J.; Plummer, A. Mechanical Properties of Titanium-Based Ti–6Al–4V Alloys Manufactured by Powder Bed Additive Manufacture. *Mater. Sci. Technol.* **2017**, *33*, 138–148. [[CrossRef](#)]
22. Ming, Q.; Lim, L.C.; Chen, Z.D. Laser Cladding of Nickel-Based Hardfacing Alloys. *Surf. Coat. Technol.* **1998**, *106*, 174–182. [[CrossRef](#)]
23. Zhang, M.; Zhang, B.; Wen, Y.; Qu, X. Research Progress on Selective Laser Melting Processing for Nickel-Based Superalloy. *Int. J. Miner. Metall. Mater.* **2022**, *29*, 369–388. [[CrossRef](#)]
24. Chen, H.; Gu, D.; Kosiba, K.; Lu, T.; Deng, L.; Xi, L.; Kühn, U. Achieving High Strength and High Ductility in WC-Reinforced Iron-Based Composites by Laser Additive Manufacturing—ScienceDirect. *Addit. Manuf.* **2020**, *35*, 101195.
25. Huang, W.; Chen, S.; Xiao, J.; Jiang, X.; Jia, Y. Laser Wire-Feed Metal Additive Manufacturing of the Al Alloy. *Opt. Laser Technol.* **2021**, *134*, 106627. [[CrossRef](#)]
26. Ostovari Moghaddam, A.; Shaburova, N.A.; Samodurova, M.N.; Abdollahzadeh, A.; Trofimov, E.A. Additive Manufacturing of High Entropy Alloys: A Practical Review. *J. Mater. Sci. Technol.* **2021**, *77*, 131–162. [[CrossRef](#)]
27. Gong, G.; Ye, J.; Chi, Y.; Zhao, Z.; Wang, Z.; Xia, G.; Du, X.; Tian, H.; Yu, H.; Chen, C. Research Status of Laser Additive Manufacturing for Metal: A Review. *J. Mater. Res. Technol.* **2021**, *15*, 855–884. [[CrossRef](#)]
28. Blakey-Milner, B.; Gradl, P.; Snedden, G.; Brooks, M.; Pitot, J.; Lopez, E.; Leary, M.; Berto, F.; du Plessis, A. Metal Additive Manufacturing in Aerospace: A Review. *Mater. Des.* **2021**, *209*, 110008. [[CrossRef](#)]
29. Naseer, M.U.; Kallaste, A.; Asad, B.; Vaimann, T.; Rassölkin, A. A Review on Additive Manufacturing Possibilities for Electrical Machines. *Energies* **2021**, *14*, 1940. [[CrossRef](#)]
30. Selema, A.; Ibrahim, M.N.; Sergeant, P. Electrical Machines Winding Technology: Latest Advancements for Transportation Electrification. *Machines* **2022**, *10*, 563. [[CrossRef](#)]
31. Hu, G.; Huang, B.; Xie, H.; Zuo, L.; Wang, N.; Li, D. Ultrasonic-Assisted Direct Writing Metal Additive Manufacturing Technique—ScienceDirect. *J. Mater. Process. Technol.* **2023**, *312*, 117830. [[CrossRef](#)]
32. Wu, T.; Liu, J.; Wang, K.; Wang, L.; Zhang, X. Microstructure and Mechanical Properties of Wire-Powder Hybrid Additive Manufacturing for High Nitrogen Steel. *J. Manuf. Process.* **2021**, *70*, 248–258. [[CrossRef](#)]
33. Yasa, E.; Kruth, J.-P.; Deckers, J. Manufacturing by Combining Selective Laser Melting and Selective Laser Erosion/Laser Re-Melting. *CIRP Ann.* **2011**, *60*, 263–266. [[CrossRef](#)]
34. Gao, B.; Zhao, H.; Peng, L.; Sun, Z. A Review of Research Progress in Selective Laser Melting (SLM). *Micromachines* **2023**, *14*, 57. [[CrossRef](#)] [[PubMed](#)]
35. Guo, S.; Li, Y.; Gu, J.; Liu, J.; Peng, Y.; Wang, P.; Zhou, Q.; Wang, K. Microstructure and Mechanical Properties of Ti6Al4V/B4C Titanium Matrix Composite Fabricated by Selective Laser Melting (SLM)—ScienceDirect. *J. Mater. Res. Technol.* **2023**, *23*, 1934–1946. [[CrossRef](#)]
36. Li, Y.; Liu, S.; Zhi, H.; Yang, X.; Zhang, J.; Wang, Y. In-Situ Generation of High-Strength AISI 1045 Steel with SiO<sub>2</sub> Nano-Precipitation by Selective Laser Melting (SLM). *J. Manuf. Process.* **2023**, *94*, 374–386. [[CrossRef](#)]
37. Tonelli, L.; Fortunato, A.; Ceschini, L. CoCr Alloy Processed by Selective Laser Melting (SLM): Effect of Laser Energy Density on Microstructure, Surface Morphology, and Hardness. *J. Manuf. Process.* **2020**, *52*, 106–119. [[CrossRef](#)]
38. Lan, L.; Yang, Z.; Wang, W.; Cui, Z.; Hao, X. Effect of Initial Powder Particle Size on Densification Behavior and Mechanical Properties of Laser Additive Manufacturing of AlCoCrFeNi<sub>2.1</sub> Eutectic High-Entropy Alloy. *Powder Technol.* **2023**, *420*, 118379. [[CrossRef](#)]
39. Měsíček, J.; Čegan, T.; Ma, Q.-P.; Halama, R.; Skotnicová, K.; Hajnýš, J.; Juřica, J.; Krpec, P.; Pařáč, M. Effect of Artificial Aging on the Strength, Hardness, and Residual Stress of SLM AlSi10Mg Parts Prepared from the Recycled Powder. *Mater. Sci. Eng. A* **2022**, *855*, 143900. [[CrossRef](#)]
40. Xiang, H.; Chen, G.; Zhao, W.; Wu, C. Densification Behavior and Build Quality of Duplex Stainless Steel Fabricated by Laser Powder Bed Fusion. *Metals* **2013**, *13*, 741. [[CrossRef](#)]
41. Dwivedi, S.; Rai Dixit, A.; Kumar Das, A. Wetting Behavior of Selective Laser Melted (SLM) Bio-Medical Grade Stainless Steel 316L. *Mater. Today Proc.* **2022**, *56*, 46–50. [[CrossRef](#)]

42. Weingarten, C.; Buchbinder, D.; Pirch, N.; Meiners, W.; Wissenbach, K.; Poprawe, R. Formation and Reduction of Hydrogen Porosity during Selective Laser Melting of AlSi10Mg. *J. Mater. Process. Technol.* **2015**, *221*, 112–120. [[CrossRef](#)]
43. Wang, L.; Wang, S.; Hong, X. Pulsed SLM-Manufactured AlSi10Mg Alloy: Mechanical Properties and Microstructural Effects of Designed Laser Energy Densities. *J. Manuf. Process.* **2018**, *35*, 492–499. [[CrossRef](#)]
44. Ma, M.; Wang, Z.; Zeng, X. A Comparison on Metallurgical Behaviors of 316L Stainless Steel by Selective Laser Melting and Laser Cladding Deposition. *Mater. Sci. Eng. A* **2017**, *685*, 265–273. [[CrossRef](#)]
45. Zhong, Y.; Liu, L.; Wikman, S.; Cui, D.; Shen, Z. Intragranular Cellular Segregation Network Structure Strengthening 316L Stainless Steel Prepared by Selective Laser Melting. *J. Nucl. Mater.* **2016**, *470*, 170–178. [[CrossRef](#)]
46. Wang, D.; Song, C.; Yang, Y.; Bai, Y. Investigation of Crystal Growth Mechanism during Selective Laser Melting and Mechanical Property Characterization of 316L Stainless Steel Parts. *Mater. Des.* **2016**, *100*, 291–299. [[CrossRef](#)]
47. Kim, S.-T.; Kim, S.-Y.; Lee, I.-S.; Park, Y.-S.; Shin, M.-C.; Kim, Y.-S. Effects of Shielding Gases on the Microstructure and Localized Corrosion of Tube-to-Tube Sheet Welds of Super Austenitic Stainless Steel for Seawater Cooled Condenser. *Corros. Sci.* **2011**, *53*, 2611–2618. [[CrossRef](#)]
48. Li, H.; Jiang, Z.; Zhang, Z.; Yang, Y. Effect of Grain Size on Mechanical Properties of Nickel-Free High Nitrogen Austenitic Stainless Steel. *J. Iron Steel Res. Int.* **2009**, *16*, 58–61. [[CrossRef](#)]
49. Sohrabi, M.J.; Mirzadeh, H.; Sadeghpour, S.; Mahmudi, R. Grain Size Dependent Mechanical Behavior and TRIP Effect in a Metastable Austenitic Stainless Steel. *Int. J. Plast.* **2023**, *160*, 103502. [[CrossRef](#)]
50. Liang, Z.; Chen, X.; Sun, Z.; Guo, Y.; Li, Y.; Chang, H.; Zhou, L. A Study on the Compressive Mechanical Properties of 316L Diamond Lattice Structures Manufactured by Laser Powder Bed Fusion Based on Actual Relative Density. *J. Manuf. Process.* **2022**, *84*, 414–423. [[CrossRef](#)]

**Disclaimer/Publisher's Note:** The statements, opinions and data contained in all publications are solely those of the individual author(s) and contributor(s) and not of MDPI and/or the editor(s). MDPI and/or the editor(s) disclaim responsibility for any injury to people or property resulting from any ideas, methods, instructions or products referred to in the content.